International Journal of Hydrogen Energy 288 (2026) 158203

Contents lists available at ScienceDirect

International Journal of Hydrogen Energy

journal homepage: www.elsevier.com/locate/he

A comprehensive full-metal and optical engine study of hydrogen-diesel dual-fuel combustion

Mayanka Jha [a,*], Ari Ainsalo [a], Qiang Cheng [a], Joakim Kapp [a], Jennifer Schurr [a], Olli Ranta [a], Otto Blomstedt [a], Teemu Anttinen [b], Ossi Kaario [a]

[a] Department of energy and mechanical engineering, Aalto university, Otakaari 1, Espoo, 02150, Finland
[b] Agco Power, Moottorikatu 7-10, Linnavuori, 37240, Finland

ARTICLE INFO

Keywords:
Hydrogen-diesel dual-fuel combustion
Full-metal engine
Optical engine
Engine performance
Emissions

ABSTRACT

This study experimentally investigates hydrogen-diesel dual-fuel combustion using full-metal and optical single-cylinder research engines. Premixed hydrogen is ignited by a diesel pilot over a range of engine speeds, lambda (λ), combustion phasing, and hydrogen energy shares (HES), at constant total fuel energy input. The full-metal engine achieves stable operation up to 50% HES, with ~50% CO_2 reduction and gross indicated thermal efficiency of ~44%–47%. At the highest-soot condition, 50% HES reduces soot by ~80%, while NO_x and H_2O increase by up to ~66%. Exhaust gas temperature decreases by ~4%–5% with increasing HES. AHRR analysis shows increasing hydrogen influence on the mixing-controlled stage beyond ~30% HES. Optical measurements show delayed NFL and OH* signal appearance and increasing IDT with HES, opposite to the full-metal trend. This difference may be attributed to the combined influence of in-cylinder thermal conditions and injector-dependent mixture formation.

1. Introduction

The clean energy transition is challenging the transportation sector to reduce or eliminate greenhouse gas emissions. Internal combustion engine (ICE) based industries remain central in this shift due to their high power density, efficiency, reliability, cost-effectiveness, operational simplicity, broad power range, and rapid start-up capabilities [1,2]. However, to ensure the continued relevance of engines, it is essential to develop advanced combustion strategies that comply with increasingly stringent emission regulations. A key pathway in this effort is the replacement of conventional fossil fuels with carbon-neutral or carbon-free alternatives. Among these, hydrogen has emerged as a particularly promising candidate due to its zero carbon content, high flame speed, wide flammability limits, favourable diffusion characteristics, high specific energy density, and potential for improved thermal efficiency [3–7].

However, the development of hydrogen-fuelled engines poses significant challenges, as the properties that make hydrogen attractive, such as low minimum ignition energy, high diffusivity, and high flame speed, also lead to undesirable combustion phenomena, including pre-ignitions, backfire, or knock [8]. This underscores the need for detailed investigations of hydrogen enrichment under engine-relevant conditions to inform strategies that effectively address these challenges.

Between the two dominant engine types, compression ignition (CI) and spark ignition (SI), CI engines are recognized for achieving high indicated thermal efficiency (ITE) and lower carbon dioxide emissions (CO_2) emissions. However, CI engines exhibit a greater propensity for producing nitric oxides (NO_x) and soot compared to SI engines [9]. Despite their advantages in efficiency and CO_2 emissions, mitigating these additional emission challenges remains important. In this context, incorporating hydrogen into CI engines can markedly reduce or eliminate carbon-based emissions such as CO_2, soot and total hydrocarbons. Nevertheless, the high autoignition temperature of hydrogen (~858 K [10,11]) is hard to achieve by compression alone (without leading to abnormal combustion such as knock), necessitating the use of high-reactive fuel with lower auto-ignition temperature, such as diesel (~523 K [10]), as an ignition promoter. Furthermore, hydrogen enrichment offers a pragmatic pathway for transitioning from conventional diesel operation towards hydrogen-based engines, while leveraging and enhancing existing infrastructure. These considerations collectively underpin the adoption of dual-fuel (DF) strategies. DF strategies have been widely explored for introducing carbon neutral gaseous fuels such as methane or natural gas, into conventional diesel engines [12–15], thereby providing a foundation for extending such concepts to hydrogen.

* Corresponding author.
E-mail address: mayanka.jha@aalto.fi (M. Jha).

https://doi.org/10.1016/j.ijhydene.2026.158203
Received 22 June 2026; Received in revised form 7 October 2026; Accepted 16 October 2026
0360-3199/© 2026 The Authors. Published by Elsevier Ltd on behalf of Hydrogen Energy Publications LLC. This is an open access article under the CC BY license (http://creativecommons.org/licenses/by/4.0/).

Nomenclature

AHRR	Apparent Heat Release Rate
ATDC	After Top Dead Center
CAD	Crank Angle Degrees
CA05	CAD where 5% of total heat releases
CA50	CAD where 50% of total heat releases
CD	Combustion Duration
CFD	Computational Fluid Dynamics
CI	Compression Ignition
CL	Chemiluminescence
CO	Carbon monoxide
CO_2	Carbon dioxide
COV	Coefficient Of Variation
CR	Compression Ratio
DBTDC	Degrees Before Top Dead Center
DF	Dual-Fuel
EGR	Exhaust Gas Recirculation
EGT	Exhaust Gas Temperature
EHVA	Electro-Hydraulic Valve Actuation
FTIR	Fourier Transform Infrared Spectroscopy
HES	Hydrogen Energy Share
IDT	Ignition Delay Time
IMEP	Indicated Mean Effective Pressure
ITE_g	Gross Indicated Thermal Efficiency
MFC	Mass Flow Controller
MSS	Micro Soot Sensor
NFL	Natural Flame Luminosity
NI	National Instruments
NO_x	Nitric Oxide
SD	Standard Deviation
SOC	Start of combustion
SOI	Start of injection
TDC	Top Dead Center
λ	Lambda
λ_g	Gas Lambda

To more deeply understand the role of hydrogen in a DF strategy Tsujimura and Suzuki [16] conducted experiments with a single cylinder engine across multiple speeds and load conditions. They observed improved thermal efficiencies and reduced unburnt hydrogen emissions, with a moderate rise in NO_x emissions, at high loads and hydrogen fractions. However, pre-ignitions became frequent when hydrogen energy share (HES) exceeded 50% under high load conditions. Sharma and Dhar [17] reported that the maximum HES attainable without inducing knock is governed by compression ratio (CR) . Consequently, several studies [18–21] have sought to increase the permissible HES in diesel-hydrogen DF engines while remaining within normal-combustion constraints. These efforts typically involved fixing parameters such as CR or engine loads, or adopting low-temperature combustion strategies to define feasible hydrogen substitution limits. However, these approaches often introduced trade-offs, including decreased indicated thermal efficiency or elevated NO_x emissions.

A key challenge in hydrogen-fuelled ICE, whether adopting spark or pilot fuel-assisted ignition, is the substantial production of NO_x. This increase in NO_x is attributed to the elevated combustion temperature, oxygen concentration, and residence time in hydrogen combustion [22–25].

Given that the objective is net zero emissions, rather than solely eliminating carbon based emissions, it is essential to investigate mitigation strategies. In their review, Ma and Sun [26], concluded that primary strategies to reduce NO_x emission generation should involve either reducing the in-cylinder combustion temperature or the oxygen concentration. Consequently, some have developed mitigation techniques grounded in these concepts. Bose and Maji [27] conducted an experimental study on single cylinder diesel-engine using a hydrogen-diesel blend, where exhaust gas recirculation (EGR) was applied to reduce NO_x emissions. Their comparative study varied EGR ratio of 0%, 10% and 20% with a constant hydrogen flow rate of 0.15 kg/h. The results indicated that the NO_x emissions decreased with increasing EGR, while other emissions such as CO_2, CO and even smoke increased due to the oxygen-deficient environment created by EGR. It was further observed that even the engine performance decreased. Similar trends were reported by Nag et al. [28] and Rahman et al. [29]. A numerical study by Abuelnour et al. [30] on a hydrogen-diesel DF engine further reinforced these experimental findings. Khairallah and Koylu [31] used chemical kinetics integrated with 3D CFD to analyse the performance and emission characteristics of DF diesel-hydrogen engine. They compared EGR and N_2 dilution as NO_x mitigation strategies. Consistent with the prior findings, their results showed that both methods reduce NO_x emissions by creating an oxygen deficient environment, but concurrently lead to increased CO_2 and CO emissions, while also reducing thermal efficiency. Subramanian et al. [32] experimentally compared hot EGR, N_2, and CO_2 dilution in a water cooled hydrogen-gasoline engine. They found N_2 dilution is most effective for balancing NO_x reduction and thermal efficiency, followed by hot EGR, with CO_2 dilution performing the worst. The study concluded that dilution effects are more effective than thermal effects for optimizing NO_x emissions and thermal efficiency. Tang et al. [33] employed CFD to investigate the effects of dilution gases (N2 + Ar) in water-cooled hydrogen engine. Argon was introduced to mitigate the thermal efficiency loss, typically associated with N_2 dilution, as previously observed by Wang et al. [34] in spark ignition CNG engine. Their findings indicated that a 17%–27% dilution rate, with 80%–90% of diluent composed of Ar achieves an optimal trade-off between NO_x reduction and thermal efficiency. Szwaja [35] found that, while both EGR and lean mixtures reduce NO_x emissions in SI hydrogen engines, EGR is more effective at suppressing knock.

Water injection is another promising solution to reduce the NOx emissions. Chintala and Subramanian [36] investigated the use of a timed manifold water injection system to enhance HES and mitigate NO_x emission levels in a hydrogen-diesel DF engine. Their findings suggested that increasing specific water consumption enabled HES to rise from 20% to 39%, accompanied by a 37% reduction in NO_x, though with a marginal increase in carbon based emissions. Serrano et al. [37] reported the reduction of NO_x with increased amount of water injection in a hydrogen-diesel DF engine. However, they did not suggest a corresponding rise in other carbon-based emissions. Novella et al. [38] further suggested that water injection is as equally effective as high EGR to control NO_x, while offering the additional benefit of mitigating autoignition and knocking. Dhyani and Subramanian [39] found water injection more effective than cooled EGR in achieving backfire-free and ulta-low NO_x level in hydrogen SI engines. Additionally, Chintala and Subramanian [40] experimentally demonstrated that water injection strategy also enables higher HES, within knock-safe limits.

The reviewed literature highlights both the benefits and challenges of increasing HES in engines. Various strategies address NO_x and abnormal combustion, often at the cost of efficiencies, other emissions or added system complexity.

However, most studies are performed under fixed or coupled operating conditions, where variations in HES are inherently linked with changes in combustion phasing and total fuel energy. This obscures the systematic isolation of hydrogen influences. As a result, it becomes difficult to distinguish its independent contributions from those of combustion phasing and total fuel energy. A few studies, such as [41,42], have partially addressed this issue by employing fixed CA50 (CAD where 50% of total heat releases) and/or constant total fuel energy in direct hydrogen injection (DI) engines. Nevertheless, comparable systematic investigations remain scarce for port fuel injected (PFI) hydrogen CI engines. Although DI has attracted increasing attention because of its potential to improve power density and mitigate abnormal combustion phenomena such as backfire [22], PFI remains an attractive research configuration owing to its homogeneous mixture

Table 1
Summary of representative hydrogen-fuelled engine studies highlighting the research gaps addressed in the present work.

Year	Reference	Research configuration	Main contribution	Research gap
2009	[27]	Experimental, Single-cylinder CI engine	Demonstrated NO_x reduction using EGR in hydrogen–diesel dual-fuel combustion.	Reduced NO_x was accompanied by lower thermal efficiency and/or higher carbon-based emissions; combustion phasing and total fuel energy were not systematically controlled.
2014	[36]	Experimental, Single-cylinder CI engine	Investigated water injection to increase the allowable HES while reducing NO_x emissions.	Requires additional hardware while the independent effects of combustion phasing and total fuel energy remain unresolved.
2015	[18]	Experimental, Single-cylinder CI engine	Investigated the influence of compression ratio on the allowable hydrogen substitution limit.	Hydrogen effects remained coupled with operating conditions such as total energy and combustion phasing.
2017	[16]	Experimental, Single-cylinder CI engine	Investigated hydrogen substitution over a range of engine speeds and loads; reported improved thermal efficiency together with increased NO_x emissions and pre-ignition at HES > 50%.	Independent effects of hydrogen could not be isolated from changes in combustion phasing and total fuel energy.
2018	[17]	Numerical	Investigated the combined influence of HES and compression ratio on combustion, performance and emissions; identified the dependence of optimum HES on compression ratio.	Combustion phasing was not systematically controlled.
2018	[19]	Experimental, multi-cylinder CI engine	Investigated hydrogen enrichment under low and medium load operating conditions while evaluating the effects of diesel injection pressure, EGR and injection strategy.	Effect of hydrogen enrichment remained coupled with combustion phasing and total fuel energy.
2019	[20]	Experimental, four cylinder CI engine	Investigated hydrogen enrichment under multiple loads; reported hydrogen substitution limit based on observed backfire at multiple loads.	Lacked independent assessment of the effects of controlling combustion phasing and total fuel energy.
2021	[41]	Experimental, Single-cylinder CI engine	Investigated H_2–diesel dual direct injection under fixed CA50 and constant total fuel energy; demonstrated accelerated initial combustion with hydrogen addition.	Limited to direct hydrogen injection; did not investigate the influence of advanced or retarded CA50 on performance, emissions and combustion characteristics.
2024	[38]	Numerical	Investigated water injection as a strategy for NO_x reduction and knock mitigation; reported water injection to be better at resisting knock than EGR	Lacked establishing the relationship between combustion phasing and emissions.
2025	[42]	Experimental, Six-cylinder SI engine	Investigated direct hydrogen injection in an SI engine under fixed CA50; evaluated the influence of equivalence ratio, spark timing and injection timing.	Limited to spark-ignition operation with direct hydrogen injection; constant total fuel energy was not maintained.

preparation, lower system complexity, and implementation cost [43]. Furthermore, insights obtained from PFI combustion studies provide an important reference for the development and interpretation of future DI combustion strategies [44].

A summary of representative hydrogen-fuelled engine studies and the corresponding research gaps is presented in Table 1. As shown in the table, previous investigations have primarily focused on hydrogen substitution limits, combustion control strategy, or NO_x mitigation individually. Whereas a systematic experimental framework that combines combustion phasing control, constant total fuel energy and complimentary optical diagnostics has remained limited.

To address these identified research gaps, the present work develops a complementary experimental framework that combines full-metal and optical engines to investigate PFI hydrogen-diesel DF combustion under constant total fuel energy conditions. The full-metal engine employs CA50 control, which constrains global combustion phasing and enables the systematic assessment of hydrogen effects on ignition and burn rate evolution. Under these conditions, the following parameters are systematically varied while minimizing confounding effects associated with phasing shifts.

1. Engine speed
2. HES, and
3. Lambda values

In addition, a complementary optical engine configuration is employed, operating under fixed diesel start of injection (SOI) strategy with deliberately reduced CR and skip-firing operation to lower in-cylinder thermal conditions. This configuration enables direct visualization of hydrogen-diesel combustion evolution while preserving the natural coupling between ignition and in-cylinder conditions under hydrogen enrichment.

In summary, the two engine configurations serve complementary roles, guiding the primary objectives of this study:

1. To determine the operational limits of hydrogen-diesel DF engine for optimized performance, emissions and combustion stability through key parameter interactions in a full-metal engine.
2. To visually investigate hydrogen-diesel combustion under reduced CR and low-temperature conditions using an optical engine, elucidating the fundamental ignition and flame development evolution.

2. Experimental setup and methodology

2.1. Research engines

Figs. 1 and 2 illustrate the full-metal and optical research engines employed in this study, whereas Table 2 summarizes the key specifications of both engines and their associated auxiliary systems for

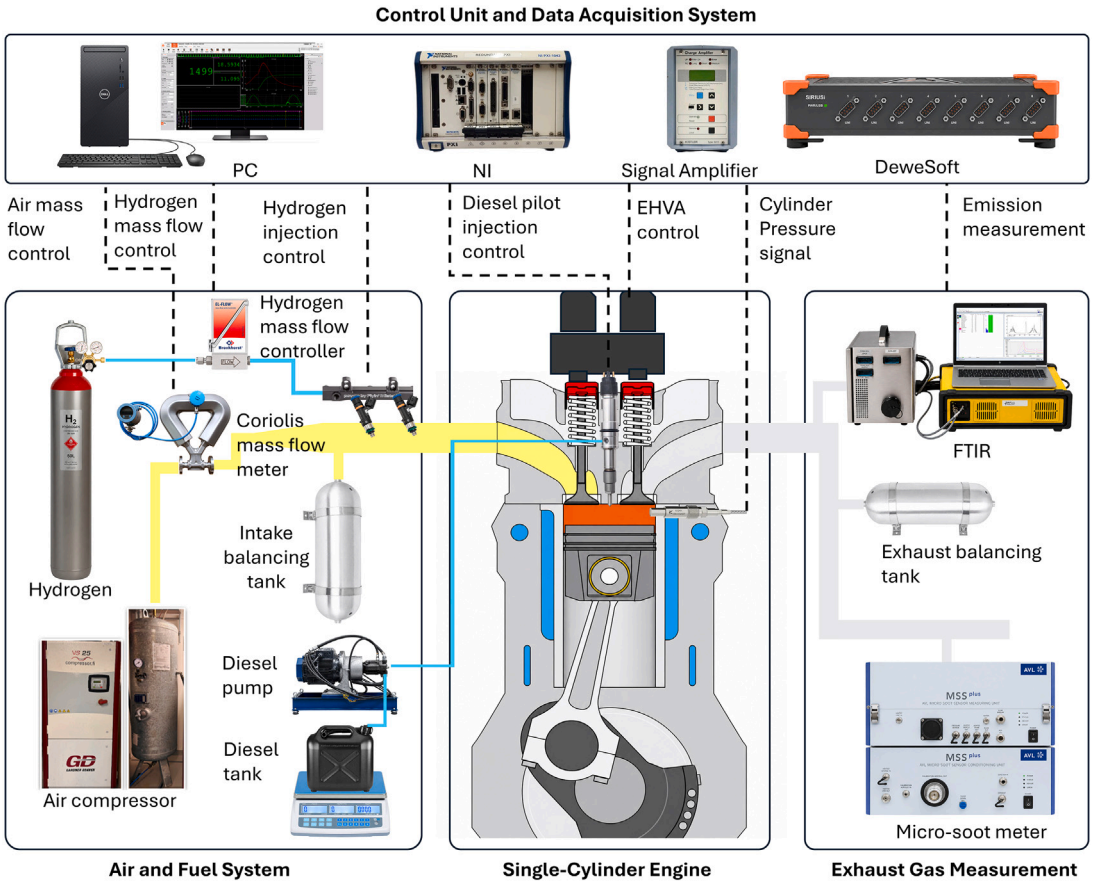


Fig. 1. Schematic representation of full-metal research engine setup.

experimental testing. While both share the same fundamental design, they differ in CR, presence of emission measurement devices, and inclusion of an optical piston. In addition, the piston designs differ between the two engines. The full-metal engine uses an industrial diesel piston bowl. The optical engine uses a flat optical piston (window) secured by a shallow metal ring. This results in an effectively shallow-bowl geometry. Despite these differences, hydrogen was introduced into both engines using port fuel injection (PFI) strategy. A mass flow controller was employed upstream of the injectors to accurately regulate the prescribed hydrogen mass flow rate and ensure repeatable fuel supply. The port injectors controlled the timing and duration of hydrogen delivery. The diesel mass flow rate was determined from a gravimetric injector calibration performed prior to the experiments. A calibration curve relating injector energizing duration (control input) to the injected fuel mass per cycle was then established and used to calculate the diesel mass flow rate. This calibration curve was subsequently used to determine the injector energizing duration corresponding to each test point.

Both research engines are equipped with a dynamometer and frequency converters to regulate and maintain the desired engine speed. Additionally, both engines are equipped with a flame arrestor positioned upstream the hydrogen injectors, near intake air manifold to mitigate the risk of flame flash back. An in-cylinder pressure transducer enables detailed combustion analysis, including cylinder pressure, heat release rate, combustion phasing and indicated power by capturing high-resolution pressure data (0.2 CAD) synchronized with crankshaft position. These fast-response measurements are acquired using DeweSoft data acquisition software.

In the full-metal engine, 50 consecutive cycles were recorded by DeweSoft for each test point. Real-time continuous measurement data from various sensors (e.g., mass flow meters, thermocouples, intake air pressure sensors) were monitored, controlled, and visualized using LabVIEW, a graphical programming environment developed by National Instruments (NI). Gaseous emissions from the full-metal engine exhaust were sampled using the Fourier Transform Infrared (FTIR) system and recorded via Calcmet software. Particulate emissions were measured using Micro Soot Sensor (MSS) and recorded with AVL software, which was also synchronized with the LabView program.

The optical engine was not fitted with any emission measurement devices as the primary objective was to capture visual data. Combustion characteristics were observed through an optically accessible piston and pressure transducer mounted in the cylinder head. The optical piston provided an 85 mm window to 111 mm combustion chamber. The non-optical control and data acquisition were identical to those used in the full-metal engine. Natural flame luminosity (NFL) and OH* chemiluminescence (CL) were captured simultaneously with a high speed colour and a monochrome camera respectively. Additionally, the monochrome camera was equipped with an UV intensifier and a low pass filter to capture OH* CL. The cameras were positioned approximately 90° apart, with a beam splitter installed in front to ensure equal light distribution to both sensors during simultaneous operation. The optical components are summarized in Table 3.

2.2. Test cases and procedure

The study commenced with experiments on the full-metal engine, and test cases have been outlined in Table 4. These cases were sequentially designed and executed in the order presented in the table. In the first phase (Table 4 CASE A) of the experiments, the goal was to understand hydrogen enriched combustion at different engine speeds. Therefore, the engine was operated at three different speeds. To enable a fair comparison across these speeds, the total fuel energy and intake

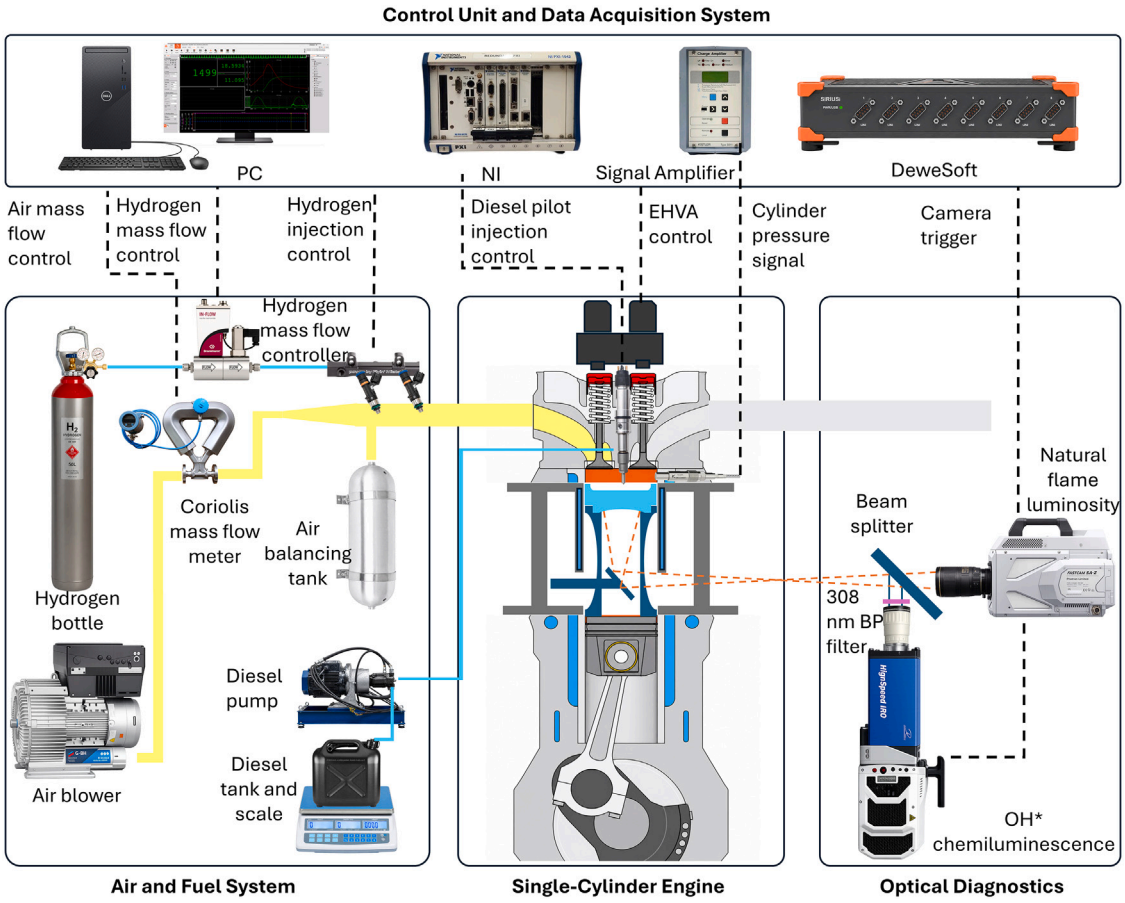


Fig. 2. Schematic of optical research engine setup.

Table 2
Specifications of research engines and associated auxiliaries.

Parameters	Full-metal engine	Optical engine
Engine type	4-stroke, single cylinder engine	4-stroke, single cylinder engine
Displacement volume (dm^3)	1.25	1.40
Bore ×stroke (mm^2)	110 × 132	111 × 145
Valve system	EHVA	EHVA
Air induction system	Air compressor + Coriolis mass flow meter + PID control valve	Air blower + Coriolis mass flow meter
Diesel injection system	Common rail + electrically driven fuel pump + solenoid direct injector	Common rail + electrically driven fuel pump + piezoelectric direct injector
Diesel injector nozzle-hole diameter (μm)	163	105
Hydrogen injection system	Mass flow controller + 2 port fuel injectors	Mass flow controller + 2 port fuel injectors
Emission measurement devices	FTIR and MSS	–

Table 3
Specifications of imaging system in optical engine.

Device	Natural flame luminosity measurement	OH* chemiluminescence measurement
Camera	High speed colour camera (Photron Fastcam SA-Z)	High speed monochrome camera (Phantom V2012)
Intensifier	–	High speed intensifier
Filter	–	BP 308 nm ±10 nm wavelength filter
Objective lens	Nikon AF Nikkor 180 mm f/2.8	UV-enhanced 100 mm f/2.8
Resolution (width x height)	768 x 768 pixels	768 x 640 pixels
Frame rate	32 KHz	32 KHz

air mass flow rate per cycle was kept equal. Furthermore, at each of these speeds, the HES was swept from 0%–50% in a step of 10%. The gas duration was adjusted to achieve the required HES in accordance with the specified mass flow rate. The desired hydrogen energy share at constant total fuel energy was achieved by varying the diesel injection duration and hydrogen mass flow rate, while maintaining a constant 1000 bar diesel injection pressure throughout the experiments. At each HES, CA50 was fixed at 10°, 8° and 6° CAD by adjusting the SOI (reported throughout this study as the electronic injection command). This approach was designed to isolate key combustion characteristics

Table 4
Experimental test matrix for full-metal engine.

Fuel share (energy %)	Engine speed (RPM)	Total fuel energy (kJ/cycle)	Total fuel energy (MJ/h)	Intake air mass flow (g/cycle)	Intake air mass flow rate (kg/h)	Diesel injection pressure (bar)	Diesel injection duration (ms)	CA50 (CAD)	Gas lambda (λ_g)	Global lambda (λ)
CASE A: Effect of hydrogen enrichment at multiple speeds										
Diesel	1000		80		40					
(100%–50%)	1500	2.66	120	1.33	60	1000	0.88–0.65	10, 8, 6	17.49–3.50	1.47-1.59
+ H_2 (0%–50%)	2000		160		80					
CASE B: Effect of lambda on emissions										
Diesel				1.33	40				3.50	1.59
(50%)	1000	2.66	80	2	60	1000	0.65	10, 8, 6	5.25	2.39
+ H_2 (50%)				2.66	80				7	3.19

Table 5
Experimental test matrix for optical engine.

Fuel share (energy %)	Engine speed (RPM)	Total fuel energy (MJ/h)	Intake air mass flow (kg/h)	Diesel injection pressure (bar)	Diesel injection duration (ms)	Start of injection (DBTDC)	Gas lambda (λ_g)	Global lambda (λ)
CASE C: Impact of hydrogen enrichments on combustion at fixed SOI								
Diesel (100%–60%) + H_2 (0%–40%)	1000	60	30	1000	0.82 - 0.53	8	17.65 –4.41	1.46 –1.27

Table 6
Measurement systems and corresponding manufacturer specifications used in the present study.

Measured quantity	Full-metal engine	Optical engine
Cylinder pressure	AVL pressure transducer (Linearity≤ ±0.3%)	Kistler pressure transducer (Linearity≤ ±0.4%)
Exhaust gas temperature	K-type thermocouple (Accuracy ±2 °C)	K-type thermocouple (Accuracy ±2 °C)
Hydrogen flow rate	Bronkhorst MFC (Accuracy ±(0.5% Rd + 0.1% FS))	Bronkhorst MFC (Accuracy ±(0.5% Rd + 0.1% FS))
Air flow rate	Emerson coriolis flow meter (Flow accuracy ±0.25%)	Rheonik coriolis flow meter (Flow accuracy ±0.1%)
Gaseous emissions	FTIR (Linearity < ±2%)	–
Soot concentration	MSS (Resolution ≤ 0.01 mg/m^3)	–

influenced by hydrogen enrichment, including ignition delay, combustion duration and peak heat release rates across different test points. These three CA50 values were selected to enable evaluation of early and late combustion behaviour. The study was limited to 50% HES in the full-metal engine. At 60% HES ($\lambda_g \sim 2.92$), the target CA50 could no longer be maintained despite iterative adjustments to diesel injection timing. Instead, combustion phasing progressively advanced and was accompanied by a rapid pressure rise, preventing reliable data acquisition.

Based on the findings from the first phase, the second phase (Table 4 CASE B) was developed with the objective of reducing NO_x emissions. In this phase, only one of the engine speeds was considered (see Section 3.2 for explanation of choosing this particular engine speed). At this engine speed, a lambda sweep was conducted by varying the air mass flow rate at the highest HES of 50%. As in CASE A, CA50 was fixed at 10°, 8° and 6° CAD, with total fuel energy being kept constant throughout the tests.

In the full-metal engine tests, each operating point was run for about 2.5-3 min following the injection of both fuels, to allow the system to reach steady-state conditions. Subsequently, in-cylinder pressure data were recorded at every 0.2 CAD using DeweSoft over 50 consecutive engine cycles for each test condition . The cycle-averaged pressure traces were then used for the combustion analysis. To minimize high frequency noise, a low-pass Butterworth filter was applied to the pressure traces.

The recorded in-cylinder pressure data were analysed using the first law of thermodynamics to calculate the apparent heat release rate (AHRR) [45].

Table 5 presents the test matrix for the optical engine. The operating conditions differ slightly from those of the full-metal engine (see Table 4). Such differences were implemented to ensure lower in-cylinder temperatures and prevent potential damage to the optical piston and other sensitive components. To further reduce in-cylinder temperatures and protect the optical components, the engine was operated in skip firing mode, consisting of one fired cycle followed by seven skipped cycles. For each test point, a total of ten fired cycles were synchronized and triggered to record images with both cameras. Meanwhile, DeweSoft recorded the non-optical data for both fired and unfired cycles at each test condition. To systematically investigate the effect of hydrogen on the combustion behaviour, the energy share was varied from 0%–40%, in 10% increments with a fixed diesel injection timing (Table 5 CASE C) at a constant engine speed of 1000 RPM. Consistent with the full-metal engine tests, the total fuel energy and air mass flow rate were maintained constant throughout the tests.

2.3. Measurement accuracy and statistical variability

The accuracy associated with the experimental measurements was assessed using both the manufacturer-specified performance characteristics of the measurement systems and the statistical variability of the combustion measurements.

The continuously measured quantities, including exhaust gas temperature (EGT), gaseous emissions, soot concentration, and fuel/air flow rates, were recorded after the engine had reached steady-state operating conditions, as described in Section 2.2. Their accuracy is therefore represented by the manufacturer specifications of the corresponding measurement systems rather than statistical cycle-to-cycle

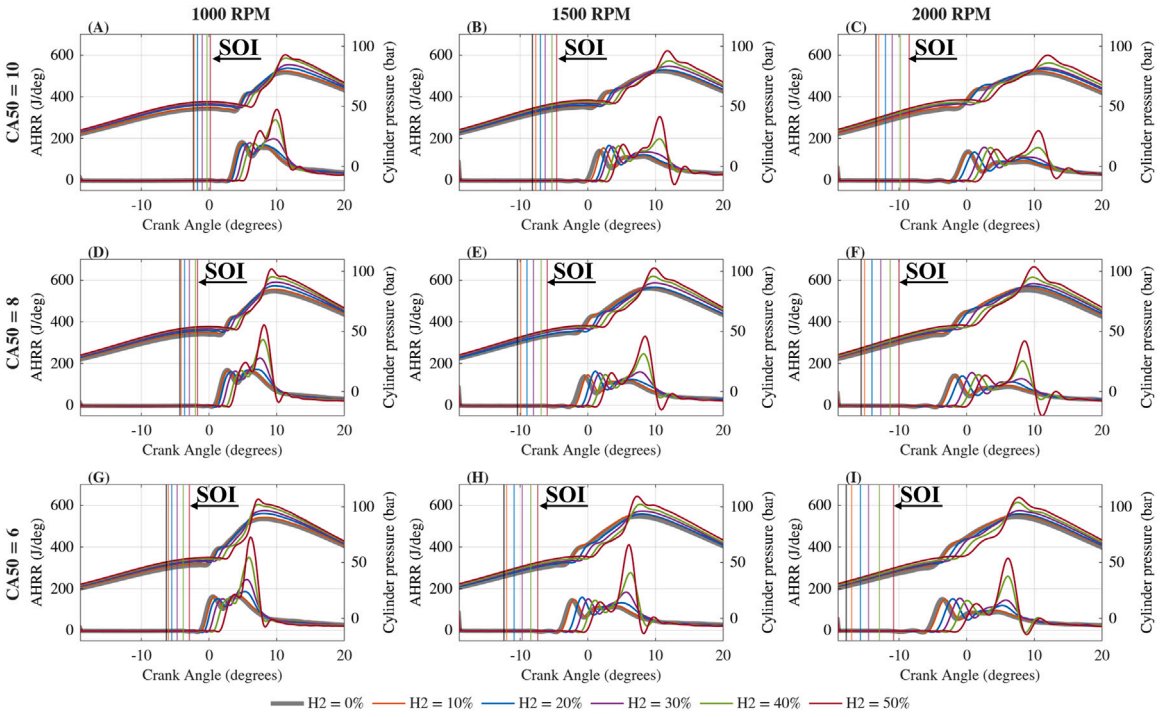


Fig. 3. Crank-angle dependence of cylinder pressure and AHRR for different HES, engine speed, and combustion phasing.

variability. The principal measurement systems and their specifications are summarized in Table 6.

The combustion parameters were calculated from the cycle-averaged in-cylinder pressure traces. These include ignition delay time (IDT), combustion duration (CD), gross indicated thermal efficiency (ITE_g), AHRR, and other pressure-derived quantities. Since these quantities are derived from high-speed in-cylinder pressure measurements, their variability was quantified using the 50 consecutive engine cycles recorded at each operating condition. Depending on the parameter, it is presented as either ±SD error bars or IMEP-based cyclic variation metrics.

In addition, a repeatability assessment was performed for measurements acquired on two different dates under a representative operating condition (Figure S4 Supplementary Material). The difference between repeated measurements remained below 3.5%, for both cylinder-pressure-derived quantities and thermocouple/emission measurements, indicating good experimental repeatability.

3. Results and discussions

3.1. Combustion analysis in the full-metal engine

Combustion behaviour in full-metal engine (Table 4) was assessed using AHRR and cylinder pressure analyses. Fig. 3 illustrates these profiles for CASE A under the tested HES, engine speeds, and CA50 conditions.

The AHRR profiles exhibit two peaks with distinct characteristics (refer Fig. 3 A-I, left axis) for all tested engine speeds and CA50 conditions. The first peak, which increases gradually, corresponds to the premixed diesel combustion with some entrained premixed hydrogen. In contrast, the second peak, exhibiting a steeper rise, is associated with the mixing-controlled combustion phase. Following the second peak, combustion continues into the late combustion phase at a lower AHRR.

Except for the pure diesel case (HES = 0%), the mixing-controlled phase is expected to be influenced by the presence of premixed hydrogen as well. Since the heat released during the mixing-controlled phase is primarily governed by the fuel vapour-air mixing process [45], hydrogen is expected to enhance the second AHRR peak through its influence on the fuel vapour-air mixing process [46]. This enhancement could result from either accelerated flame propagation of hydrogen or end-gas autoignition. Nevertheless, it is difficult to distinguish whether the second AHRR peak results from end-gas autoignition or accelerated flame propagation solely based on the measured in-cylinder pressure traces. In addition, the remaining unburnt fuel (hydrogen + diesel) may continue to burn during the late combustion phase, appearing as small AHRR peaks.

However, up to ~30% HES (indicated by the purple solid lines in Fig. 3 A-I, left y-axis), the peak magnitudes of the premixed-controlled and mixing-controlled dominated AHRR remain nearly equal. This suggests that low HES does not significantly affect the mixing-controlled phase. Nevertheless, at and beyond 40% HES (indicated by the green solid lines in Fig. 3 A-I, left y-axis), the second AHRR peak increases more rapidly than the first. This behaviour may be associated with the high flame speed of richer premixed hydrogen, which could increasingly influence the overall combustion rate beyond a certain energy threshold. In addition, the increase in AHRR with higher HES is reflected in the corresponding rise in peak cylinder pressure (refer Fig. 3 A-I, right y-axis). Consistent with the AHRR trends, a sharp rise in peak cylinder pressure is observed beyond 30% HES, at a crank angle close to that of the second AHRR peak. These findings suggest that HES of at least 40% of the total fuel energy is required to trigger a transition towards an accelerated burn rate during the mixing-controlled phase in the DF full-metal engine under the CASE A conditions (see Table 4, CASE A).

The influence of combustion phasing, shown in Fig. 3 (for clarity see panels A, D and G) further highlights the distinct roles of the two combustion modes. The data shows that only the second AHRR peak increases with advanced phasing, while the first AHRR peak decreases.

This behaviour can be explained by the injection strategy required to achieve an early CA50. Advancing CA50 necessitates an early start of diesel injection, meaning the spray is introduced further away from TDC, into a lower pressure and density environment. Under these conditions, atomization, vaporization and air entrainment are less effective. Although the earlier SOI provides a longer premixing period, these less favourable spray-development conditions may reduce the fraction of fuel reaching a combustible mixture state by the time of ignition.

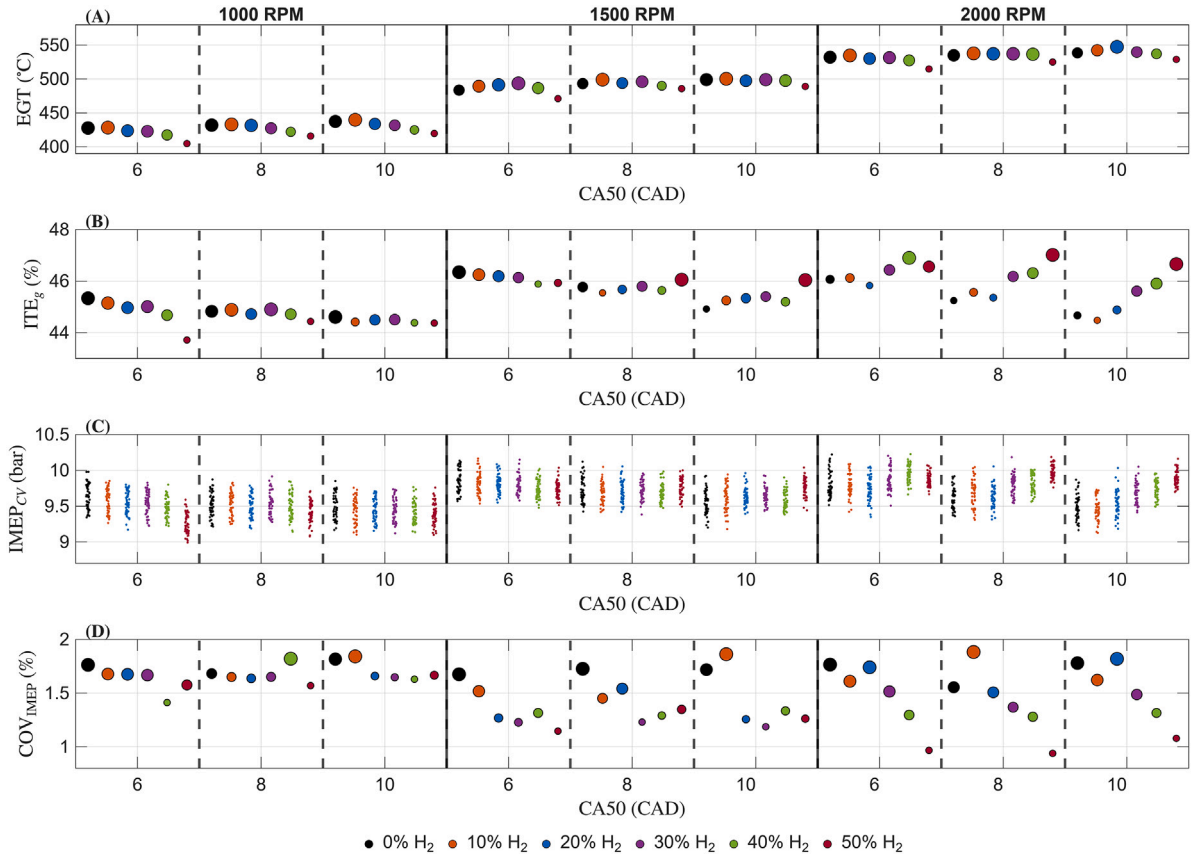


Fig. 4. **(A)** EGT **(B)** ITE$_g$ **(C)** Cyclic variations (CV) of IMEP **(D)** COV of IMEP across different HES, engine speed and fixed CA50.

Consequently, the premixed AHRR peak diminishes, despite the globally advanced combustion phasing. In contrast, mixing controlled phase becomes more pronounced with advanced CA50. The burning rate during the mixing-controlled phase is governed by the rate at which the mixture becomes available for combustion. With an advanced fixed CA50, this burning occurs closer to TDC, where the in-cylinder conditions are more favourable for rapid combustion. This results in a more pronounced second AHRR peak. Thus, advancing CA50 preferentially promotes the mixing-controlled combustion process while suppressing the premixed AHRR peak.

The comparative analysis of AHRR versus crank angle across engine speeds in Fig. 3 reveals an unexpected trend: AHRR appears to decrease as engine speed increases. This seems counter-intuitive, given that higher speeds typically enhance turbulence intensity, promote fuel-air mixing, and are therefore expected to increase the burning rate. The contradiction arises because AHRR is evaluated with respect to crank angle rather than time.

As engine speed increases, the duration of 1 CAD decreases, resulting in less fuel being burned per crank-angle and consequently a lower CAD-based AHRR. To properly account for differences in combustion rate, AHRR was reassessed as a function of time. Figure S1 (Supplementary materials) illustrates the temporal AHRR profiles for 0%, 30% and 50% HES across all engine speeds, along with corresponding CA50 values. When analysed on time basis, AHRR increases with engine speed, consistent with the expected physical response to elevated turbulence levels. Furthermore, the influence of engine speed and fixed CA50 on the second AHRR peak becomes pronounced above 30% HES. Even when analysed temporally, the results consistently indicate that substantial modifications to overall combustion characteristics behaviour occur only when hydrogen contributes above ~30% of the total fuel energy.

3.2. Performance and emission analysis in the full-metal engine

The effects of combustion phasing (CA50), engine speed and HES on (A) EGT, (B) ITE$_g$, (C) cyclic variations of indicated mean effective pressure (IMEP$_{CV}$), and (D) coefficient of variation (COV) are summarized in Fig. 4.

As shown in Fig. 4 A, EGT exhibits an increasing trend with rising speed. This is because higher engine speeds result in shorter cycle durations. Consequently, there is less residence time for the burned gases to transfer heat to the cylinder walls before exhaust valve opening, thereby increasing the measured EGT [45]. In contrast, advancing or retarding CA50 within the investigated range has only a minor influence on EGT. This suggests that within the tested range, the timing of CA50 does not significantly affect the thermal energy retained within the exhaust gases. Furthermore, despite the high adiabatic temperature and fast combustion characteristics of hydrogen, EGT was lowest at highest HES. This behaviour is attributed to the earlier completion of combustion, as evidenced by progressive advancement of CA90 (CAD where 90% of total heat releases) with increasing HES (Figure S2, Supplementary materials). Consequently, the burned gases have additional time to expand before exhaust gas valve opening, thereby reducing the measured EGT.

In contrast to the monotonic relationship between EGT and HES observed in Fig. 4 A, Fig. 4 B exhibits a non-linear association between ITE$_g$ and HES. At 1000 RPM with CA50 fixed at 6 CAD and HES at 50%, ITE$_g$ attains its minimum value. At the same HES, it reaches its maximum at 2000 RPM with CA50 fixed at 8 CAD. IMEP$_{CV}$ and the corresponding COV remain minimal, as shown in Fig. 4 C and D respectively. Therefore, the efficiency variation observed at high hydrogen content cannot be attributed to cyclic variations. Nevertheless, ITE$_g$ remains nearly constant across all test points. This confirms that the total energy per cycle was maintained constant, as targeted in the

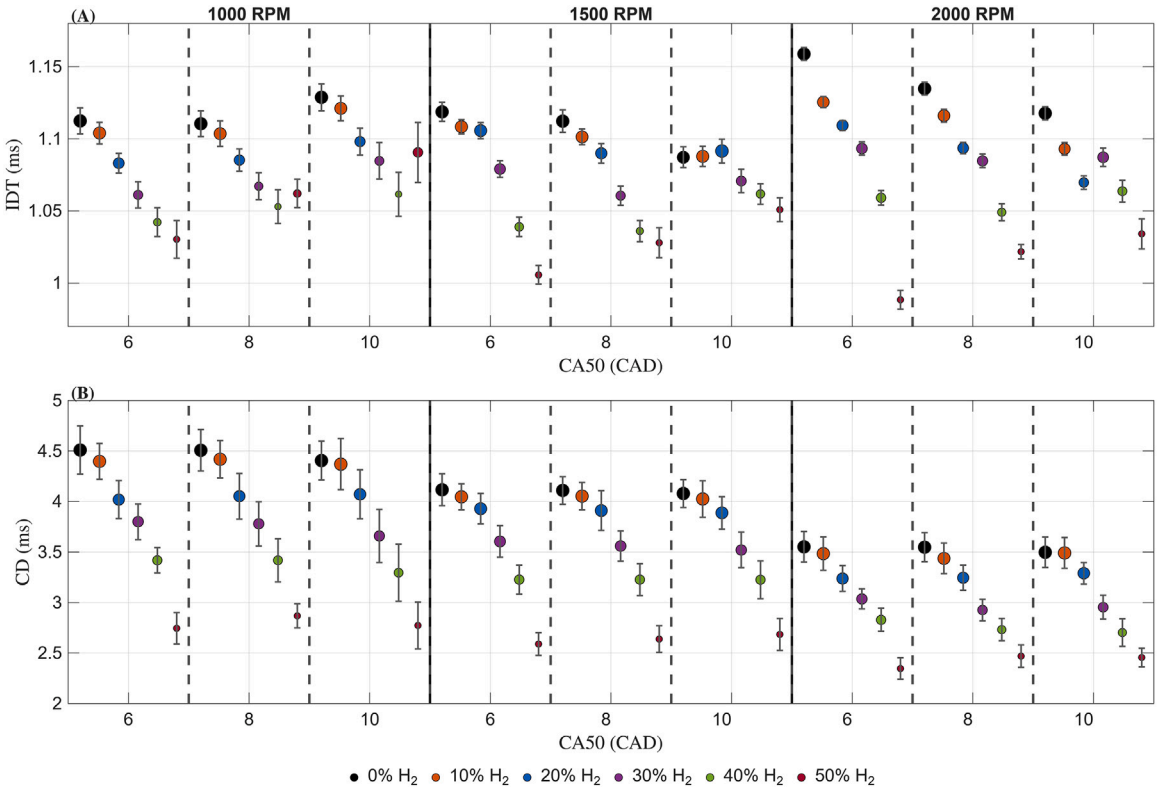


Fig. 5. **(A)** IDT **(B)** CD as a function of HES, engine speed and CA50.

experimental test matrix (Section 2.2 and 4). Overall, $IMEP_{CV}$ and COV_{IMEP} indicate improved stability with hydrogen at higher engine speeds. For the investigated conditions (see Table 4 Case A), HES above 30% appears to represent a threshold beyond which engine stability improves with increasing speed.

Fig. 5 A presents the IDT trends. In the present study, IDT is defined as the difference between CA05 (CAD where 5% of total heat releases) and SOI. Despite minor non-monotonic variations between adjacent HES levels, the overall tendency is towards shorter IDT with increasing HES under fixed CA50 conditions. The trends reflect the active participation of hydrogen from the initial stages of combustible mixture formation itself. Since both CA50 and total fuel energy were maintained constant, the shorter IDT with increasing HES indicates accelerated reaction rates. As a result, interval between SOI and SOC (Start of combustion)/ CA05 decreases to maintain the target CA50. Furthermore, IDT does not seem to exhibit a linear dependence on engine speed under the fixed combustion phasing conditions examined in the full-metal engine. In contrast, the CD (Fig. 5 B) which is defined as difference between CA90 and CA05, is significantly influenced by both engine speed as well as HES. As engine speed increases the CD decreases due to enhanced turbulence, which improves mixing, and flame propagation. Consequently, combustion is completed more rapidly. At all engine speeds, CD further decreases with increasing HES because of high flame speed and rapid reactivity of hydrogen.

The influence of CA50, HES, and engine speed on (A) NO_x emissions (B) CO_2 emissions and (C) H_2O emissions concentration is illustrated in Fig. 6. An increase in HES and earlier CA50 leads to elevated NO_x emissions, primarily due to higher in-cylinder temperatures that promote thermal NO_x formation [42]. Conversely, NO_x emissions tend to decrease with increasing engine speed, attributed to reduced residence time for nitrogen oxidation due to shorter cycle durations. CO_2 emissions decline with increasing HES reflecting the depleting carbon content of the fuel mixture, and appear largely unaffected by combustion phasing. A slight reduction in CO_2 is also observed at higher engine speed, likely due to shorter cycle durations that limit the residence time available for complete carbon oxidation. This is supported by the corresponding increase in CO emissions (Figure S3, Supplementary materials). Consequently, the reduced oxidation time can also promote higher emissions of unburnt carbon species, such as soot.

Fig. 7, presents the soot emission results at (A) 1000 RPM (B) 1500 RPM and (C) 2000 RPM at defined CA50 and HES. Soot emissions decrease with increasing HES at constant engine speed and combustion phasing, indicating reduced carbon availability, with higher hydrogen substitution. However, at constant HES and CA50, soot emissions increase with engine speed, consistent with reduced oxidation time available during shorter engine cycle. Additionally, at higher engine speeds (1500 and 2000 RPM), soot emissions exhibit greater sensitivity to CA50, in contrast to the relative independence of CO_2 emissions from combustion phasing. In particular, as shown in Fig. 7 C, later combustion phasing (CA50 = 10), promotes higher soot production.

The observed soot trends can be explained by the interaction between SOI and piston bowl. Since CA50 was controlled by adjusting the SOI, achieving later CA50 required a retarded SOI (Fig. 3 C). Fuel injection therefore occurred closer to TDC, reducing the available premixing time. The modified spray-bowl interaction may also have increased local fuel accumulation through spray impingement and fuel film formation. This favoured fuel-rich regions and consequently higher soot formation. Conversely, an earlier CA50 required an advanced SOI (Fig. 3 (F,I)) . This increased the premixing time before ignition and promoted a more homogeneous mixture formation, thereby reducing soot emissions. Similar increases in soot with retarded SOI have also been reported previously [47].

In addition to carbon and nitrogen based-emissions, H_2O emissions were also measured, with corresponding trends shown in Fig. 6 C.

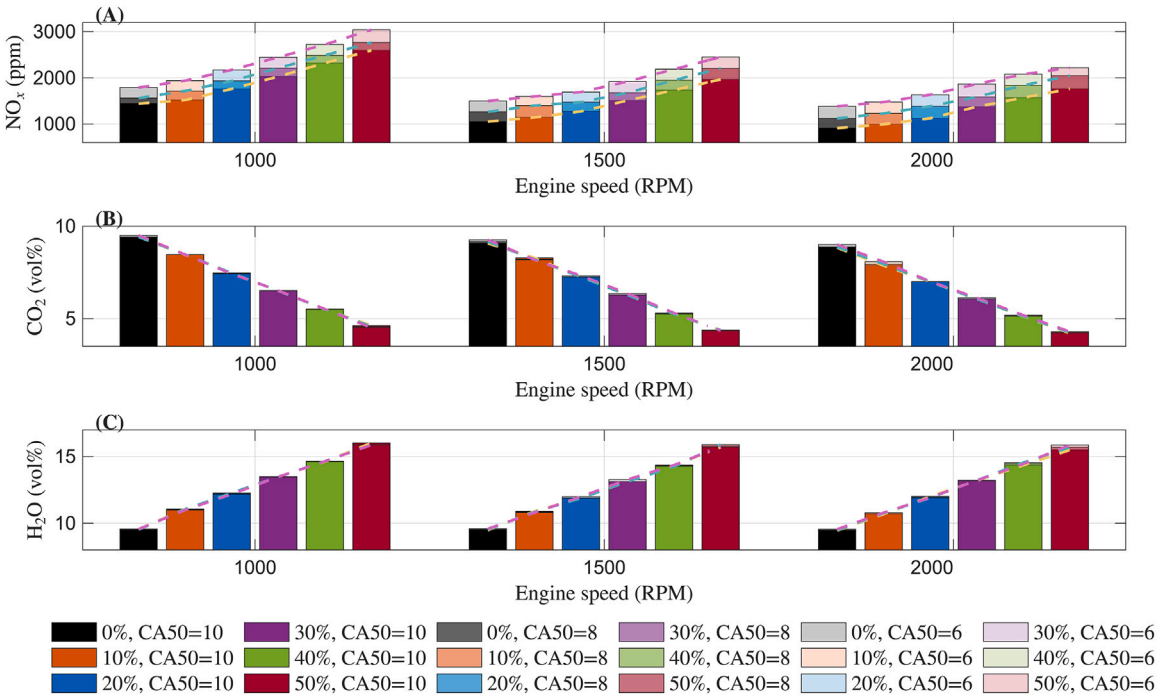


Fig. 6. **(A)** NO_x **(B)** CO_2 **(C)** H_2O emissions as a function of HES, engine speed and CA50.

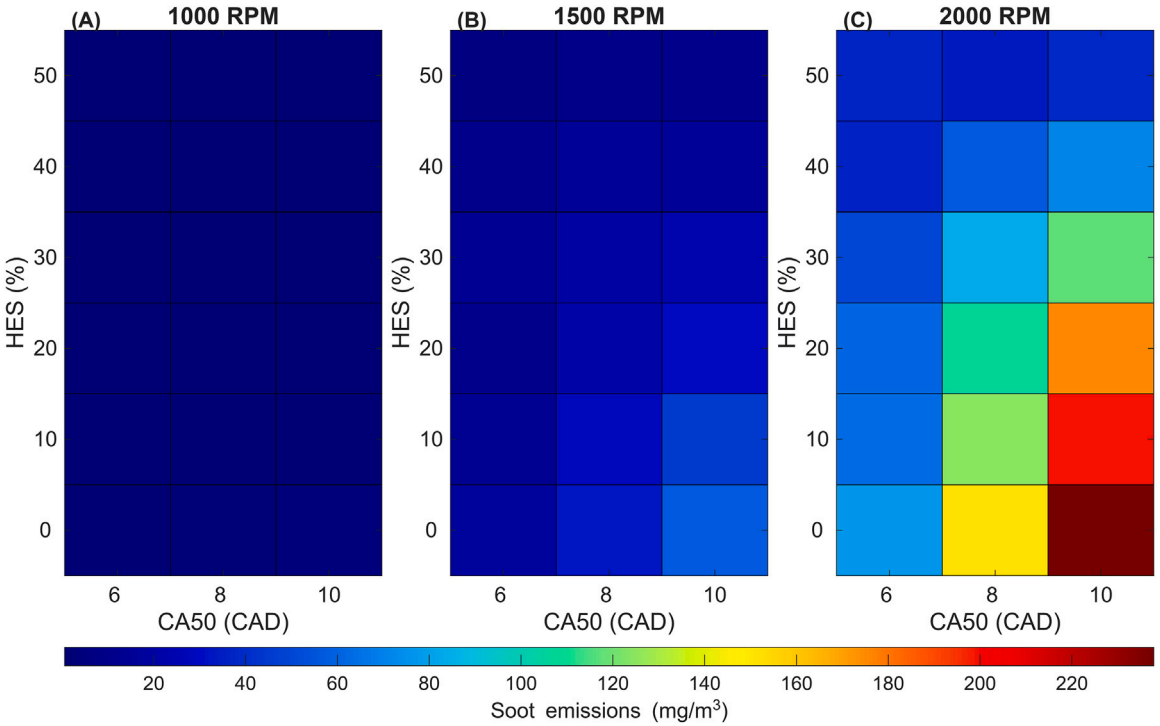


Fig. 7. Soot emissions at **(A)** 1000 RPM **(B)** 1500 RPM and **(C)** 2000 RPM as function of HES and CA50.

Similar to CO_2 emissions, H_2O emissions are primarily governed by fuel composition increasing with HES while remaining largely insensitive to combustion phasing.

A key challenge identified in the current experiments was the elevated NO_x emissions observed under low engine speed and high HES. Consequently, this operating condition was selected for developing Case B (Table 4).

The variations of (A) NO_x emissions in ppm and (B) CO_2 emissions in vol% with λ_g is shown in Fig. 8. Both NO_x and CO_2 concentrations decrease significantly with increasing λ_g. This behaviour results from the combined effect of constant total fuel energy input and increased intake air mass flow, which leads to emission dilution. However, even under leaner conditions, NO_x remains sensitive to the combustion phasing, whereas CO_2 is largely unaffected.

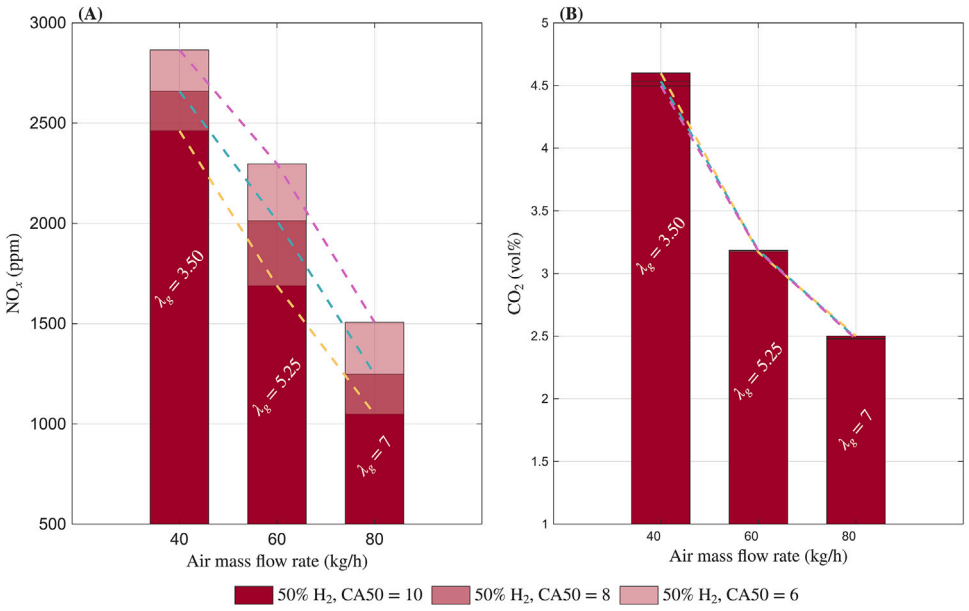


Fig. 8. **(A)** NO_x **(B)** CO_2 emissions as function of λ_g and CA50 at a constant engine speed of 1000 RPM and a HES of 50%.

3.3. Optical diagnostics of hydrogen-enriched combustion: natural flame luminosity and OH chemiluminescence analysis*

This section discusses the optical results corresponding to the test case defined in Table 5. Fig. 9 presents crank-angle resolved NFL images for varying HES, while Fig. 10 presents the OH* CL images. Images obtained from both diagnostics are shown at comparable CAD.

The NFL images (Fig. 9) show a progressive transition in dominant flame colour from yellow to blue with increasing HES. For pure diesel conditions (H_2 = 0%), the flame appears predominantly yellow, with a faint bluish background. The yellow luminosity is typically associated with blackbody radiation from soot particles, whereas the bluish flame arises from emission of excited radicals [48]. As soot originates from unburnt carbon species, these regions indicate fuel-rich (diesel-rich) zones, characteristic of diffusion-controlled combustion. In contrast, the transition to blue-dominated flames reflects reduced soot formation, which would otherwise have been obscured under strong soot radiation [49]. Thus, the emergence of a blue-dominated flame is indicative of a shift towards premixed combustion.

Although not all CAD synchronized images are presented, the complete dataset was analysed. Beyond 20% HES, soot-related luminosity, identified by bright yellow regions, becomes minimal or absent. These observations indicate that, for the present engine configuration and operating conditions, a discernible influence of premixed hydrogen emerges at or beyond a HES of ~30%, under low CR (optical, without CA50 control) conditions. In contrast, under high CR (full-metal, with CA50 control) conditions, a slightly higher HES of at least ~40% is required to observe enhancements due to premixed hydrogen. Nevertheless, the combined quantitative (Fig. 7) and visual assessments (Fig. 9) from both engines confirm that increasing HES, while maintaining constant total energy input, reduces soot emissions.

Furthermore, Fig. 9 indicates that with increasing hydrogen addition, the CAD at which NFL first becomes visible is progressively delayed. For example, at 20% HES, the first clearly visible flame appears ~0.7 CAD after CAD = 7.6 ATDC, with this delay increasing further at higher HES. This trend is also evident in the cycle-averaged NFL intensity (Fig. 11 A), where increasing HES reduces the peak NFL intensity and delays the onset of the NFL signal.

Consistent with this, the OH* CL results (Fig. 10) show a clearly detectable OH* signal at 20% HES and CAD = 7.6 ATDC, despite reduced NFL intensity. The simultaneous presence of OH* and diminished NFL signal further supports the presence of hydrogen and transition towards premixed combustion, particularly beyond 10% HES. However, even at 20% HES, the OH* signal is weaker than that observed at 10% and 0% HES for the same crank angle, although it remains clearly visible. With further increases in HES, the initial appearance of the OH* signal shifts to later CAD, indicating a corresponding increase in IDT. The cycle-averaged OH* intensity (Fig. 11 B) further confirms the progressive delay in the onset of the OH* signal with increasing HES.

The delayed appearance of both NFL and OH* signals with increasing HES is consistent with the calculated IDT based on heat release and OH* intensity (Fig. 12 A and B). The heat-release-based IDT is defined as the difference between CA05 and SOI for the cycle presented in Fig. 10. The OH*-based IDT is defined as the difference between the crank angle at which first detectable rise in the cycle-averaged OH* CL signal is observed and SOI. Overall, the optical engine results indicate that IDT increases with increasing HES. In contrast, the full-metal engine results generally show a decrease in IDT with increasing HES (see Section 3.2 and Fig. 5 A). The longer IDT in the optical engine is also reflected in the NFL images (Fig. 9). With increasing HES, the flames become progressively bluer. This is consistent with the longer premixing period associated with increased IDT.

A longer IDT in the optical engine is expected compared to the full-metal engine due to reduced CR and skip firing operation, which lower the in-cylinder temperatures (Fig. 13). For example, the calculated IDT of pure diesel case (0% HES) at 1000 RPM, increases by ~1 ms when transitioning from full-metal engine (Fig. 5 A) to the optical engine (Fig. 12 A). The difference in piston-bowl geometry may also contribute to the observed IDT difference. It can influence the interaction between the injected diesel and the surrounding H_2-air charge, as well as the local air-flow motion. The full-metal piston bowl may promote faster redistribution of the injected diesel towards the surrounding H_2-air charge. It may also modify the air-flow motion to favour faster air-diesel fuel mixing and, consequently, shorter IDT. In contrast, the shallow-bowl optical piston may result in slower redistribution of the injected fuel towards the surrounding H_2-air charge. It may also generate a less turbulent environment, leading to slower air-flow-driven mixing. These differences in piston-bowl interaction may therefore contribute to the longer IDT observed in the optical engine at constant HES and engine speed compared to the full-metal engine.

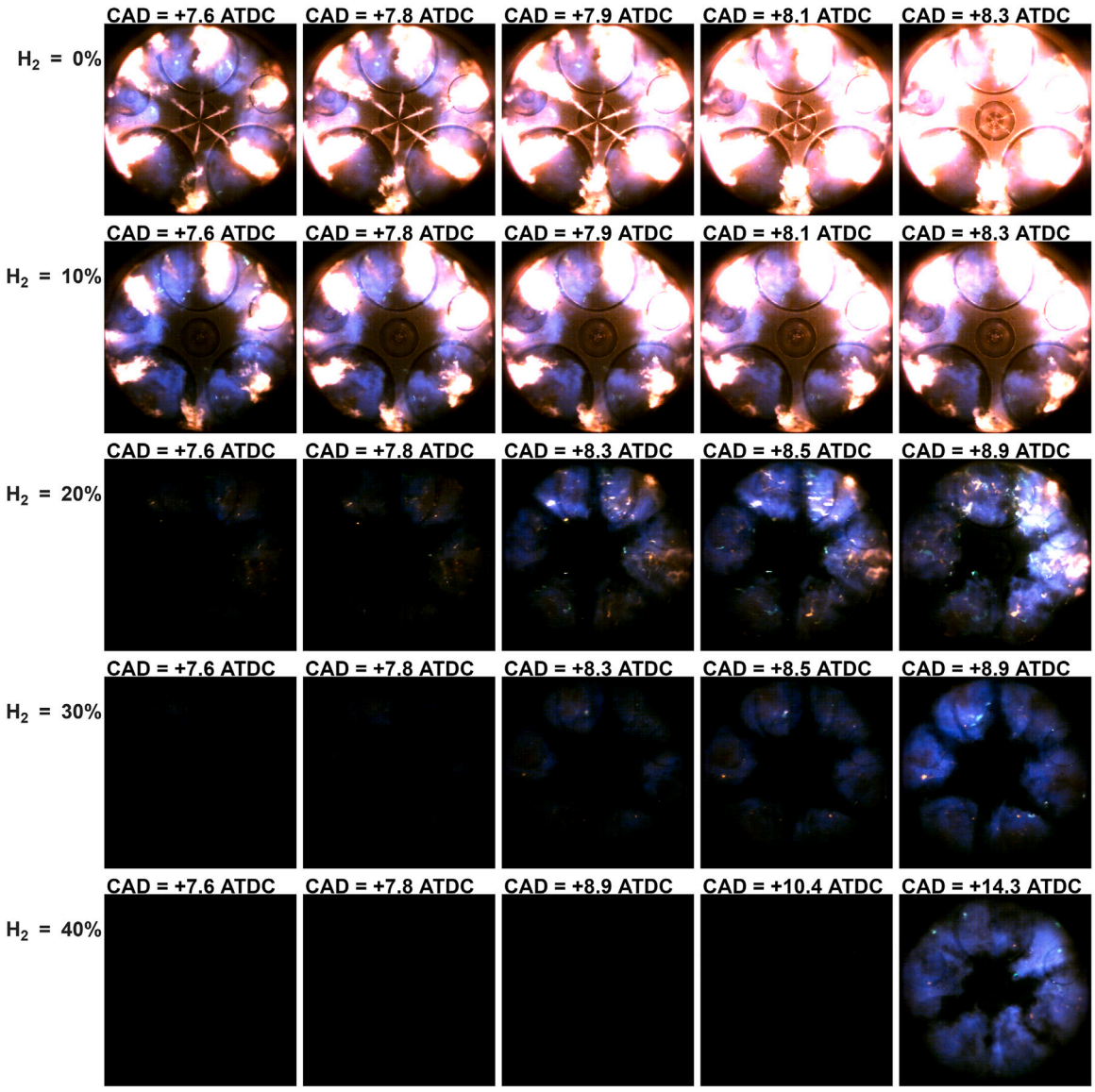


Fig. 9. Crank angle resolved evolution of natural luminosity of a hydrogen-diesel flame at an engine speed of 1000 RPM.

However, the further increase in IDT with hydrogen enrichment in optical engine appears counter-intuitive. For instance, when transitioning from pure diesel to 40% HES in the optical engine, the IDT increases from ~2.4 ms to ~3.3 ms (Fig. 12 A and B). In contrast, in the full-metal engine at 1000 RPM and across CA50 conditions, the IDT decreases from ~1.13 ms to ~1.06 ms when transitioning from pure diesel to 40% HES (Fig. 5 A).

This opposite trend highlights the sensitivity of ignition behaviour to the in-cylinder environment. In fact, based on previous studies and their own results Pinto et al. [50] highlighted that hydrogen enrichment may either reduce or increase IDT, depending on the hydrogen volume fraction and temperature conditions.

Therefore, to further investigate this behaviour, the in-cylinder temperature at the start of injection was estimated for both full-metal and optical engines assuming isentropic compression process with constant specific heat ratio. The reference crank angle was taken as the end of intake stroke (start of compression). The corresponding in-cylinder pressure was extracted from the measured pressure trace. The reference temperature was assumed to be ambient temperature (298 K). The temperature at SOI was then estimated using Eq. (1).

$$T_{SOI} = T_{ref}\left(\frac{P_{SOI}}{P_{ref}}\right)^{\frac{\gamma-1}{\gamma}} \quad (1)$$

where a constant specific heat ratio $\gamma = 1.37$ was assumed. Fig. 13 presents corresponding temperature trends. In general, the in-cylinder calculated isentropic temperature at SOI in the full-metal engine is close to ~900 K, whereas in the optical engine it remains near ~750 K.

These estimates indicate that the optical engine operates under a comparatively lower-temperature combustion environment, whereas the full-metal engine represents higher-temperature operating conditions. It was initially hypothesized that the prolonged ignition delay observed with hydrogen enrichment in the optical engine could be associated with enhanced low-temperature diesel oxidation chemistry. Under such conditions, hydrogen addition, while simultaneously reducing the diesel pilot quantity, may alter the low-temperature oxidation pathways governing diesel autoignition. Gu et al. [51] reported that hydrogen promotes reaction pathways that consume OH radicals, thereby suppressing the H-abstraction reactions responsible for *n*-dodecane decomposition and consequently increasing ignition delay.

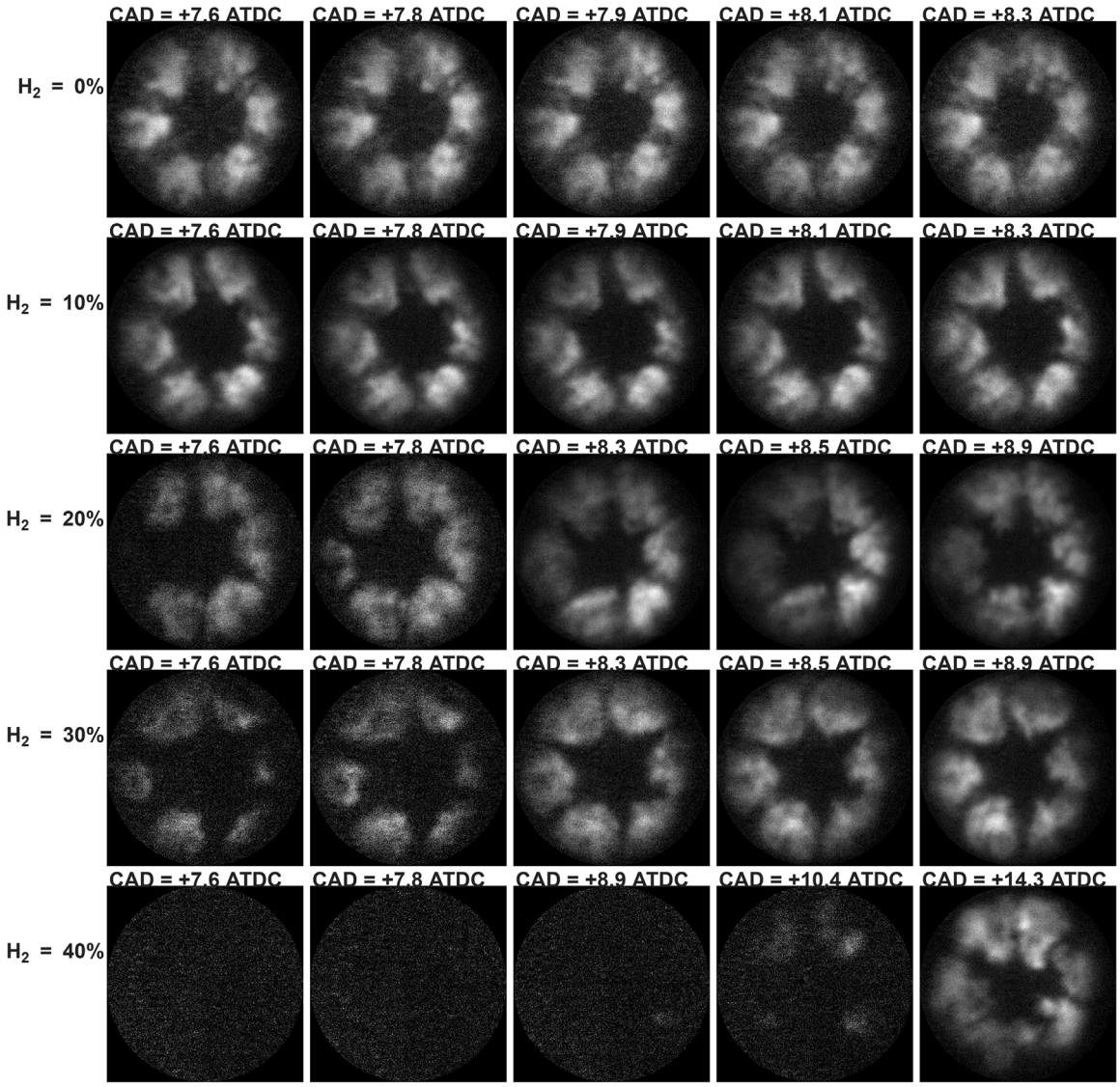


Fig. 10. Crank angle resolved evolution of OH* chemiluminescence of a hydrogen-diesel flame at an engine speed of 1000 RPM.

Similar interpretations were also reported by Hernández et al. [52] for hydrogen-diesel mixtures in a constant-volume combustion chamber. Nevertheless, low-temperature chemistry has also been reported to remain relevant at temperatures approaching 900 K [53]. Therefore, the opposite ignition-delay trends observed between the two engines cannot be explained solely by differences in in-cylinder temperature.

In addition to thermal effects, differences in diesel spray formation and local mixture preparation are also likely to influence the ignition process. The full-metal engine employs an injector with a ~1.6 times larger nozzle-hole diameter than the injector used in the optical engine. Such a configuration is expected to produce larger locally fuel-rich regions, thereby increasing the probability of forming locally reactive ignition kernels. In contrast, the finer injector employed in the optical engine is expected to generate comparatively leaner local fuel regions. Furthermore, increasing HES, reduces the oxygen concentration of the fresh charge into which the diesel pilot is injected [54]. Consequently, the local oxygen availability governing diesel autoignition is reduced. In the full-metal engine, the presence of larger locally fuel-rich regions may partially compensate for the reduction in local oxygen availability. Conversely, in the optical engine, the combined influence of lower-temperature conditions, reduced local oxygen availability, and smaller locally fuel-rich regions is likely to promote longer ignition delays. Lee et al. [55] similarly reported that sufficiently rich pilot-fuel regions are essential for successful ignition under premixed hydrogen conditions.

Accordingly, the opposite ignition-delay trends are likely governed by the combined effects of in-cylinder thermal conditions, and injector-dependent pilot-fuel mixture formation. However, further investigations are required to systematically isolate the configuration differences between the two engines and verify this hypothesis. The proposed interpretation should therefore be regarded as a literature-supported hypothesis that is consistent with the present experimental observations.

4. Conclusion

This study investigated the effects of hydrogen enrichment under different engine operating conditions, with emphasis on identifying systematically isolated relationships relevant to combustion, performance and emissions. The following are the main conclusions that can be drawn from the work:

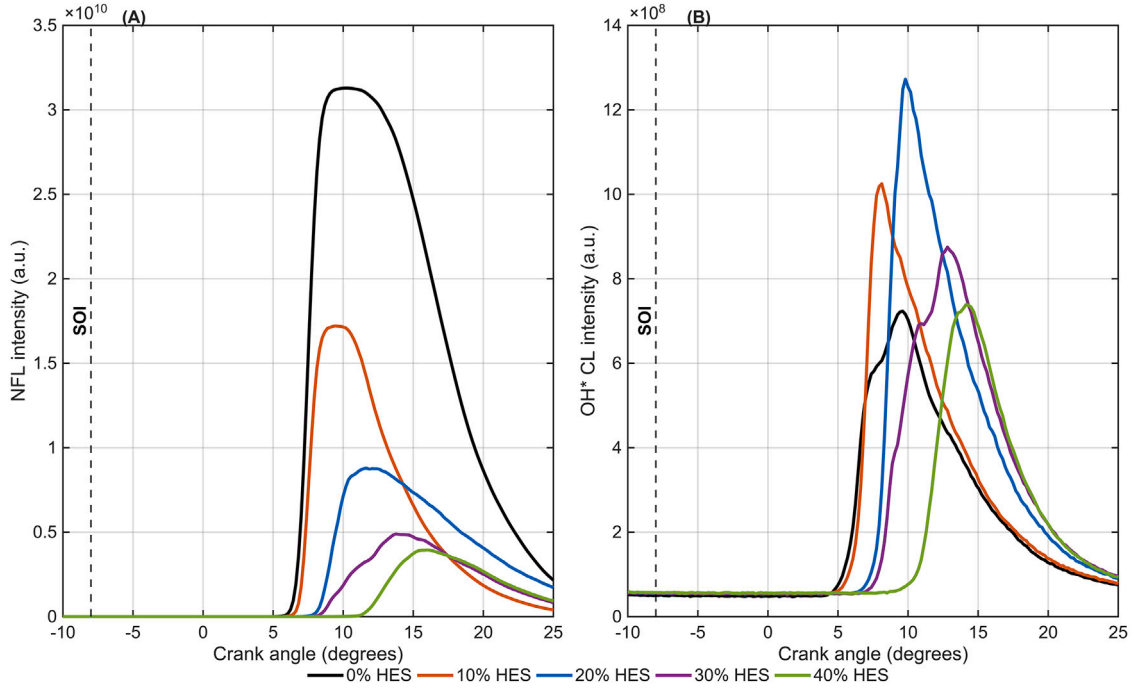


Fig. 11. Cycle-averaged **(A)** NFL intensity and **(B)** OH* CL intensity of the hydrogen-diesel flame at an engine speed of 1000 RPM for varying HES and fixed SOI of 8 DBTDC.

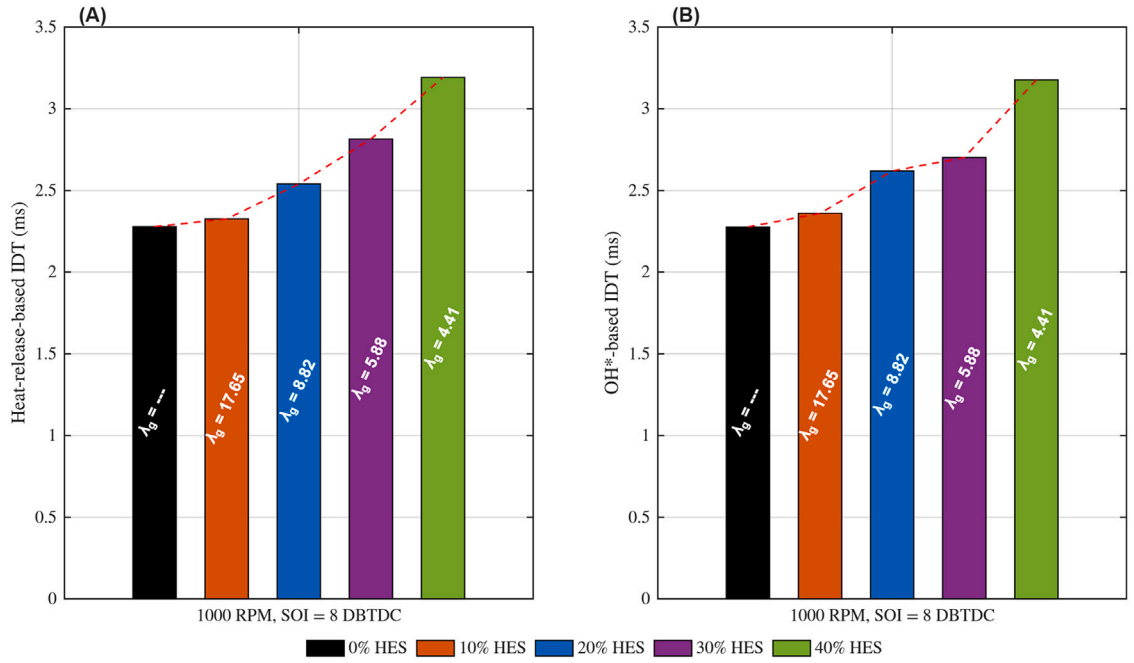


Fig. 12. **(A)** Heat-release-based IDT and **(B)** OH*-based IDT at varying HES under a constant engine speed of 1000 RPM and fixed SOI of 8 DBTDC in the optical engine.

1. Transitioning towards higher HES and earlier CA50 increased both the cylinder pressure and heat release rate at all engine speeds, reflecting the high reactivity and rapid flame propagation characteristics of hydrogen.
2. Higher HES and advanced combustion phasing also increased NO_x emissions. However, leaner operation (higher λ or λ_g) consistently reduced NO_x emissions at a given combustion phasing.
3. Increasing the HES to 50% reduced CO_2 emissions by ~50% across all combustion phasing conditions and engine speeds. In contrast, soot emissions increased with engine speed, particularly under retarded combustion phasing, with this effect being more pronounced at lower HES (< 40%).
4. Increasing HES shortened the combustion duration (CD) and reduced the exhaust gas temperature (EGT), reflecting the faster combustion characteristics of hydrogen.
5. Comparison of IDT behaviour in the full-metal and optical engines showed opposite trends with increasing HES. While IDT generally decreased with increasing HES in the full-metal engine,

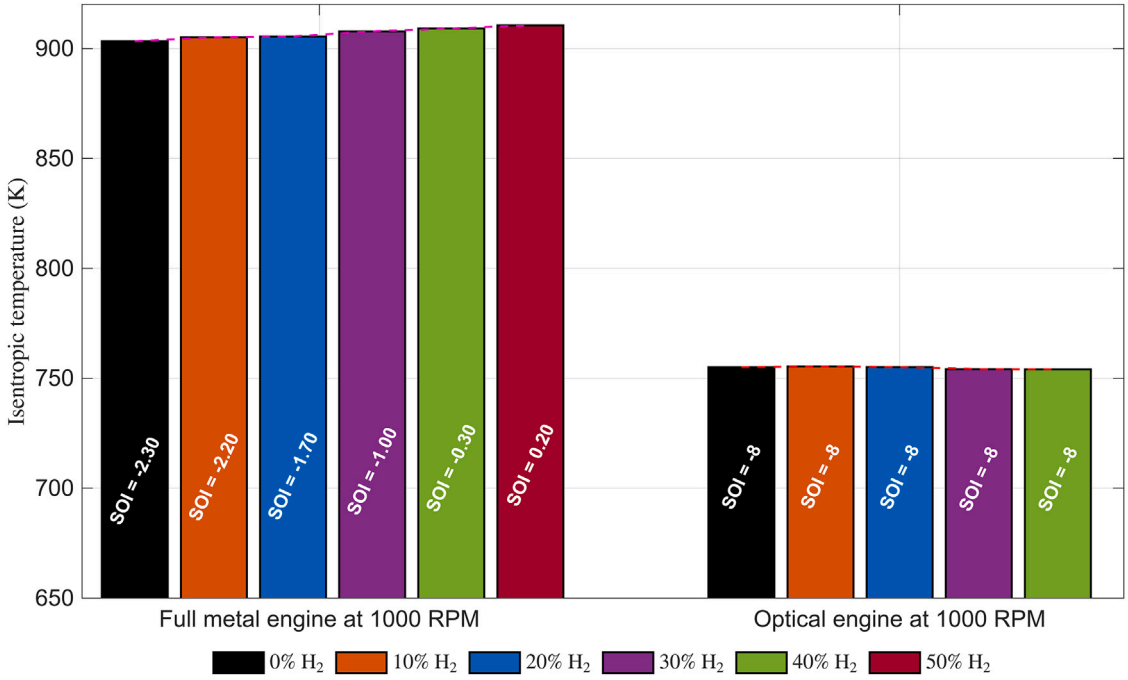


Fig. 13. Calculated isentropic in-cylinder temperatures at diesel injection timing for the full-metal and optical engine at 1000 RPM and varying HES. Full-metal engine conditions: fixed CA50 = 10 CAD; optical engine conditions: fixed SOI = 8 DBTDC.

it increased in the optical engine. Based on the present observations and supporting literature, this behaviour is hypothesized to arise from the combined influence of in-cylinder thermal conditions, and injector-dependent mixture formation.

In summary, an optimal engine condition can be considered as one that provides a reasonable trade-off between combustion stability, performance, and emissions. Considering that the objective of the present work was to maximize hydrogen substitution while maintaining stable dual-fuel operation (up to 50% HES), the following operating guidelines can be drawn:

1. At a constant load, higher engine speeds (~2000 RPM) can be operated with higher HES (~50%) to maximize ITE_g. Lower engine speeds (~1000 RPM) preferably require lower HES (~30%–40%) to maintain high ITE_g. However, HES should also be selected based on the unburnt H_2 concentration in the exhaust, particularly for multi-cylinder operation across different engine speeds and loads.
2. Combustion phasing should be maintained close to CA50 ~8 CAD, provided that stable combustion is achieved. During multi-cylinder implementation, this target should be verified against cylinder-to-cylinder combustion variability. If excessive pressure fluctuations or unstable combustion are observed, a slightly retarded combustion phasing or lower HES may provide a more robust operating strategy.
3. A $\lambda_g \sim 7$ should be targeted to provide a favourable compromise between NO_x emissions and combustion stability. Its optimum value should be established together with combustion phasing and HES to maintain stable combustion while minimizing cylinder-to-cylinder variability.
4. An engine speed of approximately 1500 rpm should be targeted to achieve a favourable compromise between combustion completeness and emissions. The suitability of this operating point should subsequently be verified over the complete engine operating map, where engine load, and cylinder-to-cylinder variations may influence the final calibration.

CRediT authorship contribution statement

Mayanka Jha: Writing – review & editing, Writing – original draft, Visualization, Methodology, Software, Investigation, Formal analysis, Data curation, Conceptualization. **Ari Ainsalo:** Writing – review & editing, Investigation. **Qiang Cheng:** Writing – review & editing, Supervision, Software, Investigation, Conceptualization. **Joakim Kapp:** Visualization, Investigation. **Jennifer Schurr:** Writing – review & editing. **Olli Ranta:** Resources, Investigation. **Otto Blomstedt:** Resources. **Teemu Anttinen:** Writing – review & editing. **Ossi Kaario:** Writing – review & editing, Supervision, Methodology, Funding acquisition, Conceptualization.

Declaration of Generative AI and AI-assisted technologies in the writing process

During the preparation of the work the authors used ChatGpt based on GPT 5.2 to improve the language and readability. After employing the tool, the review and editing of the content was performed by the authors according to the requirements. The authors take full responsibility for the content of the publication.

Declaration of competing interest

The authors declare the following financial interests/personal relationships which may be considered as potential competing interests: Ossi Kaario reports financial support was provided by Business Finland. Ossi Kaario reports financial support was provided by Henry Fordin Säätio. If there are other authors, they declare that they have no known competing financial interests or personal relationships that could have appeared to influence the work reported in this paper.

Acknowledgements

This work was conducted as a part of the FCPT project (ref. 9719/31/2023) supported by Business Finland. The study has also been financially supported by Henry Fordin Säätio (ref. 700873).

Appendix A. Supplementary data

Supplementary material related to this article can be found online at https://doi.org/10.1016/j.ijhydene.2026.158203.

References

[1] Liu H, Yu S, Wang T, Li J, Wang Y. A systematic review on sustainability assessment of internal combustion engines. J Clean Prod 2024;451:141996.
[2] Wang Z, Pan X, Zhang W, Zhao Y, Li H, Liu P. The development trend of internal combustion engine. In: Journal of physics: conference series, vol. 1626, 2020, 012139.
[3] Fu Z, Li Y, Wu W, Li Y, Gao W. Experimental study on the combustion and emission performance of the hydrogen direct injection engine. Int J Hydrog Energy 2024;61:1047–59.
[4] Alrazen HA, Talib AA, Adnan R, Ahmad K. A review of the effect of hydrogen addition on the performance and emissions of the compression–Ignition engine. Renew Sustain Energy Rev 2016;54:785–96.
[5] Saravanan N, Nagarajan G, Sanjay G, Dhanasekaran C, Kalaiselvan K. Combustion analysis on a DI diesel engine with hydrogen in dual fuel mode. Fuel 2008;87(17–18):3591–9.
[6] Saravanan N, Nagarajan G. Performance and emission studies on port injection of hydrogen with varied flow rates with diesel as an ignition source. Appl Energy 2010;87(7):2218–29.
[7] Hamdan MO, Selim MY, Al-Omari S-A, Elnajjar E. Hydrogen supplement co-combustion with diesel in compression ignition engine. Renew Energy 2015;82:54–60.
[8] Falfari S, Cazzoli G, Mariani V, Bianchi GM. Hydrogen application as a fuel in internal combustion engines. Energies 2023;16(6):2545.
[9] Martin J, Boehman A. Mapping the combustion modes of a dual-fuel compression ignition engine. Int J Engine Res 2022;23(9):1453–74.
[10] Verhelst S, Wallner T. Hydrogen-fueled internal combustion engines. Prog Energy Combust Sci 2009;35(6):490–527.
[11] White C, Steeper R, Lutz AE. The hydrogen-fueled internal combustion engine: a technical review. Int J Hydrog Energy 2006;31(10):1292–305.
[12] Ahmad Z, Kaario O, Qiang C, Larmi M. Effect of pilot fuel properties on lean dual-fuel combustion and emission characteristics in a heavy-duty engine. Appl Energy 2021;282:116134.
[13] Papagiannakis R, Hountalas D. Combustion and exhaust emission characteristics of a dual fuel compression ignition engine operated with pilot diesel fuel and natural gas. Energy Convers Manage 2004;45(18–19):2971–87.
[14] Carlucci AP, De Risi A, Laforgia D, Naccarato F. Experimental investigation and combustion analysis of a direct injection dual-fuel diesel–natural gas engine. Energy 2008;33(2):256–63.
[15] Ahmad Z, Kaario O, Qiang C, Vuorinen V, Larmi M. A parametric investigation of diesel/methane dual-fuel combustion progression/stages in a heavy-duty optical engine. Appl Energy 2019;251:113191.
[16] Tsujimura T, Suzuki Y. The utilization of hydrogen in hydrogen/diesel dual fuel engine. Int J Hydrog Energy 2017;42(19):14019–29.
[17] Sharma P, Dhar A. Compression ratio influence on combustion and emissions characteristic of hydrogen diesel dual fuel CI engine: Numerical study. Fuel 2018;222:852–8.
[18] Chintala V, Subramanian K. Experimental investigations on effect of different compression ratios on enhancement of maximum hydrogen energy share in a compression ignition engine under dual-fuel mode. Energy 2015;87:448–62.
[19] Dimitriou P, Kumar M, Tsujimura T, Suzuki Y. Combustion and emission characteristics of a hydrogen-diesel dual-fuel engine. Int J Hydrog Energy 2018;43(29):13605–17.
[20] Castro N, Toledo M, Amador G. An experimental investigation of the performance and emissions of a hydrogen-diesel dual fuel compression ignition internal combustion engine. Appl Therm Eng 2019;156:660–7.
[21] Chintala V, Subramanian K. An effort to enhance hydrogen energy share in a compression ignition engine under dual-fuel mode using low temperature combustion strategies. Appl Energy 2015;146:174–83.
[22] Stepień Z. A comprehensive overview of hydrogen-fueled internal combustion engines: Achievements and future challenges. Energies 2021;14(20).
[23] Le D, Kwon H, JLee M. Numerical and experimental investigation of the correlation between inlet flow rates, temperature, and NOx emissions in pure hydrogen combustion. Appl Therm Eng 2025;259:124748.
[24] Chintala V, Subramanian K. A comprehensive review on utilization of hydrogen in a compression ignition engine under dual fuel mode. Renew Sustain Energy Rev 2017;70:472–91.
[25] Deb M, Sastry G, Bose P, Banerjee R. An experimental study on combustion, performance and emission analysis of a single cylinder, 4-stroke DI-diesel engine using hydrogen in dual fuel mode of operation. Int J Hydrog Energy 2015;40(27):8586–98.
[26] Ma D, Sun Z. Progress on the studies about NOx emission in PFI-H2ICE. Int J Hydrog Energy 2020;45(17):10580–91, AEM 2018 - Smart Materials for Hydrogen Energy.
[27] Bose P, Maji D. An experimental investigation on engine performance and emissions of a single cylinder diesel engine using hydrogen as inducted fuel and diesel as injected fuel with exhaust gas recirculation. Int J Hydrog Energy 2009;34(11):4847–54.
[28] Nag S, Sharma P, Gupta A, Dhar A. Experimental study of engine performance and emissions for hydrogen diesel dual fuel engine with exhaust gas recirculation. Int J Hydrog Energy 2019;44(23):12163–75.
[29] Rahman MA, Ruhul A, Aziz M, Ahmed R. Experimental exploration of hydrogen enrichment in a dual fuel ci engine with exhaust gas recirculation. Int J Hydrog Energy 2017;42(8):5400–9.
[30] Abuelnour M, Said M, Abuelnuor A. Numerical investigation of hydrogen-diesel dual fuel engine: Combustion and emissions characteristics under varying hydrogen concentration and exhaust gas recirculation. Fuel 2024;377:132794.
[31] Khairallah HA, Koylu UO. A computational study of in-cylinder NOx reduction strategies for a compression-ignition engine fueled with diesel/hydrogen mixtures. In: Energy sustainability, vol. 56840, American Society of Mechanical Engineers; 2015, V001T08A001.
[32] Subramanian V, Mallikarjuna J, Ramesh A. Intake charge dilution effects on control of nitric oxide emission in a hydrogen fueled SI engine. Int J Hydrog Energy 2007;32(12):2043–56.
[33] Tang Y, Xing K, Huang H, Tu Z, Wang Y, Guo X. Simulation study of N2/Ar dilution gas to improve thermal efficiency and reduce NOX emissions in hydrogen engines. Int J Hydrog Energy 2024;49:636–51.
[34] Wang Z, Zuo H, Liu Z, Li W, Dou H. Impact of N2 dilution on combustion and emissions in a spark ignition CNG engine. Energy Convers Manage 2014;85:354–60.
[35] Szwaja S. Dilution of fresh charge for reducing combustion knock in the internal combustion engine fueled with hydrogen rich gases. Int J Hydrog Energy 2019;44(34):19017–25.
[36] Chintala V, Subramanian K. Hydrogen energy share improvement along with NOx (oxides of nitrogen) emission reduction in a hydrogen dual-fuel compression ignition engine using water injection. Energy Convers Manage 2014;83:249–59.
[37] Serrano J, Jiménez-Espadafor F, López A. Analysis of the effect of the hydrogen as main fuel on the performance of a modified compression ignition engine with water injection. Energy 2019;173:911–25.
[38] Novella R, García A, Gomez-Soriano J, Fogué-Robles Á. Numerical assessment of water injection for improved thermal efficiency and emissions control in a medium-duty hydrogen engine for transportation applications. Fuel 2024;359:130455.
[39] Dhyani V, Subramanian K. Control of backfire and NOx emission reduction in a hydrogen fueled multi-cylinder spark ignition engine using cooled EGR and water injection strategies. Int J Hydrog Energy 2019;44(12):6287–98.
[40] Chintala V, Subramanian K. Experimental investigation of autoignition of hydrogen-air charge in a compression ignition engine under dual-fuel mode. Energy 2017;138:197–209.
[41] Liu X, Srna A, Yip HL, Kook S, Chan QN, Hawkes ER. Performance and emissions of hydrogen-diesel dual direct injection (H2DDI) in a single-cylinder compression-ignition engine. Int J Hydrog Energy 2021;46(1):1302–14.
[42] Piano A, Pucillo F, Millo F, Giordana S, Rapetto N, Schuette C. Experimental investigation on the optimal injection and combustion phasing for a direct injection hydrogen-fuelled internal combustion engine for heavy-duty applications. Int J Hydrog Energy 2025;100:398–406.
[43] Sun B-g, Zhang D-s, Liu F-s. Cycle variations in a hydrogen internal combustion engine. Int J Hydrog Energy 2013;38(9):3778–83.
[44] Han J, Doosje E, Seykens X, Somers L. Experimental study of H2 injection strategies in a HD engine: Comparison of PFI and LPDI. Int J Hydrog Energy 2025;178:151655.
[45] Heywood JB. Internal combustion engine fundamentals. McGraw-Hill; 1988.
[46] Duan H, Wang H, Ma C, Dou Z, Bai S, Li G, Zeng X. A focused parametric study on the influence of hydrogen jet on diesel spray combustion in a dual-fuel direct injection configuration under varying impingement conditions. Fuel Process Technol 2026;288:108475.
[47] Cheng X, Chen L, Hong G, Yan F, Dong S. Modeling study of soot formation and oxidation in DI diesel engine using an improved soot model. Appl Therm Eng 2014;62(2):303–12.
[48] Li Z, Lou C, Kumfer BM. Revealing the competitive relationship between soot formation and chemiluminescence. Combust Flame 2022;245:112335.
[49] Karnani S, Dunn-Rankin D. Visualizing ch* chemiluminescence in sooting flames. Combust Flame 2013;160(10):2275–8.
[50] Pinto G, De Souza T, Da Costa R, Roque L, Frez G, Coronado C. Combustion, performance and emission analyses of a CI engine operating with renewable diesel fuels (HVO/FARNESANE) under dual-fuel mode through hydrogen port injection. Int J Hydrog Energy 2023;48(51):19713–32.

[51] Gu S, Wehrfritz A, Hawkes ER, Wu Y, Lu T, Wang H. An analysis of the ignition of hydrogen/n-dodecane dual-fuel mixing layers at engine-relevant conditions. Proc Combust Inst 2025;41:105917.
[52] Hernández JJ, Salvador JB, Cova-Bonillo A. Autoignition of diesel-like fuels under dual operation with H2. Adv Mech Eng 2019;11(6):1687814019856781.
[53] Dahms RN, Paczko GA, Skeen SA, Pickett LM. Understanding the ignition mechanism of high-pressure spray flames. Proc Combust Inst 2017;36(2):2615–23.
[54] Xu Y, Cheng S, Tu Z, Li J. Effects of hydrogen addition in intake air on combustion and emission of diesel engines. Energy Sources, Part A: Recover Util Environ Eff 2024;46(1):1831–42.
[55] Lee T, Rajasegar R, Srna A. Understanding the interplay between pilot fuel mixing and auto-ignition chemistry in hydrogen-enriched environment. Proc Combust Inst 2024;40(1–4):105351.